# Optimizing thermal performance of hollow cylindrical latent heat storage units
## Insights into geometry-driven heat transfer enhancements

Yan, Zhongjun; Liu, Zhengxuan; Luo, Yongqiang; Pan, Shulin; Chen, Wang; Zhang, Yuan; Liang, Ke

**DOI**
10.1016/j.energy.2025.135750

**Publication date**
2025

**Document Version**
Final published version

**Published in**
Energy

Energy 322 (2025) 135750

Contents lists available at ScienceDirect

Energy

journal homepage: www.elsevier.com/locate/energy

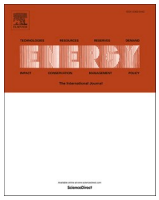

# Optimizing thermal performance of hollow cylindrical latent heat storage units: Insights into geometry-driven heat transfer enhancements

Zhongjun Yan [a], Zhengxuan Liu [b,*], Yongqiang Luo [c], Shulin Pan [a], Wang Chen [a], Yuan Zhang [a], Ke Liang [d]

[a] Department of Energy and Power Engineering, Hunan University of Humanities, Science and Technology, Loudi, 417000, China
[b] Faculty of Architecture and the Built Environment, Delft University of Technology, Julianalaan 134, 2628 BL, Delft, Netherlands
[c] School of Environmental Science and Engineering, Huazhong University of Science and Technology, Wuhan, 430074, China
[d] China Electric Power Construction Group Zhongnan Engineering Corporation Limited, Changsha, Hunan, 410014, China

ARTICLE INFO

*Keywords:*
Thermal performance improvement
Latent heat storage unit
Hot water tank
Hollow geometry
Phase change material

ABSTRACT

The thermal performance of cylindrical latent heat storage units (C-LHSUs) in hot water tanks can be improved by using a hollow geometry structure, which effectively reduces the average distance between the heated/cooled wall and the solid-liquid interface during the charging and discharging process. To comprehensively evaluate this improvement, an unconstrained melting model for phase change materials (PCMs) was developed, enabling detailed investigation of the thermal behavior of hollow geometry LHSUs (H-LHSUs). Moreover, the impact of the ratio between the inner hollow tube radius ($r$) and outer tube radius ($R$) on the charging/discharging performance of H-LHSUs was analyzed. The results demonstrated substantial enhancements in heat transfer performance for H-LHSUs compared to conventional C-LHSUs. Specifically, the average heat transfer coefficient increased by 82.9 % during charging and 176.47 % during discharging. This improvement translated to a charging rate that was 2.46 times and a discharging rate that was 3.9 times higher than those of the C-LHSU. Furthermore, the study revealed that as the $r/R$ ratio increased, both charging and discharging rates improved significantly, with the rate of heat transfer enhancement becoming more pronounced at higher $r/R$ values. This research provides actionable insights for optimizing the design of LHSUs in practical applications. It underscores the importance of balancing thermal performance gains with the associated capital costs when selecting the optimal $r/R$ ratio. The findings contribute to the advancement of energy storage technologies, offering a robust framework for improving the efficiency of thermal energy systems in hot water tanks.

Nomenclature

| | | | |
|---|---|---|---|
| | | $\rho$ | density (kg/m$^3$) |
| $A$ | mushy zone constant | $\mu$ | dynamic viscosity (kg/(m·s)) |
| $C_p$ | specific heat (J/(kg·K)) | | |
| $f$ | liquid volume fraction | *Abbreviation* | |
| $g$ | acceleration of gravity (m/s$^2$) | PCM | phase change material |
| $L$ | latent heat of fusion (J/kg) | LHSU | latent heat storage unit |
| $p$ | pressure (Pa) | HWT | hot water tank |
| $S$ | Darcy source term | H-LHSU | the hollow geometry LHSU |
| $S_L$ | energy source term | C-LHSU | The cylindrical LHSU |
| $T$ | temperature (K) | MARE | mean absolute relative error |

(*continued on next column*)

(*continued*)

| | | | |
|---|---|---|---|
| $t$ | time (s) | | |
| $u$ | solid PCM settling velocity (m/s) | *Subscripts* | |
| $V$ | velocity | s | refers to solid |
| $r$ | inner hollow tube radius | l | refers to liquid |
| $R$ | outer tube radius | *ref* | refers to reference |
| *Greek symbols* | | | |
| $\beta$ | thermal expansion coefficient (1/K) | | |
| $\varepsilon$ | computational constant | | |
| $\lambda$ | thermal conductivity (W/(m$^2$·K)) | | |

This article is part of a special issue entitled: SET2024 published in Energy.

* Corresponding author.
*E-mail address:* Z.liu-12@tudelft.nl (Z. Liu).

https://doi.org/10.1016/j.energy.2025.135750
Received 10 January 2025; Received in revised form 12 March 2025; Accepted 21 March 2025
Available online 21 March 2025

## 1. Introduction

Phase change materials (PCMs) have garnered considerable attention in solar water heating systems due to their beneficial characteristics, such as their comparatively high heat capacity and limited temperature fluctuations throughout the charging/discharging process [1]. When PCMs are encapsulated as latent heat storage units (LHSUs) and integrated with the hot water tank (HWT) of these systems, the thermal performances, such as the solar fraction and the temperature fluctuations of the supplied water, were improved [2]. However, the intrinsic challenge lies in the typically low thermal conductivities exhibited by PCMs, impeding efficient heat transfer between the LHSU and hot water [3,4]. This limitation results in relatively low charging/discharging rates for LHSUs, presenting a substantial impediment to practical applications.

In recent times, numerous strategies have been proposed to improve the heat transfer efficiency of PCMs encapsulated within LHSUs. These approaches include geometry modification [5], the incorporation of nanoparticles [6,7], the utilization of fins [8,9], and the integration of metal foams [10]. Among these approaches, geometry modification has recently emerged as a particularly effective method to enhance the thermal efficiency of LHSUs. This approach is notable as it avoids compromising heat storage capacity or necessitating costly materials with high thermal conductivities, unlike the use of nanoparticles, fins, and metal foams [11,12]. For instance, Dhaidan et al. [13] introduced a LHSU featuring an eccentric tube-in-shell configuration that shifts the center of the inner heated tube downward. Their findings revealed that an eccentricity parameter of 0.5 led to an 18.7 % decrease in charging time when compared to the concentric design. Seddegh et al. [14] introduced a conical tube-in-shell latent heat accumulator to utilize the benefits of natural convection. Their results indicated that, when compared to the cylindrical design, the PCM encapsulated within the conical geometry melted approximately 12 % faster during the charging process. These investigations underscore the significant impact of geometry modification on enhancing the heat transfer mechanism of PCMs, thereby improving the charging and discharging efficiency of LHSUs.

To date, there are only a few studies that specifically have focused on geometry modification to enhance heat transfer of the PCM, especially in situations where the PCM is encapsulated in the LHSU within HWTs. In this scenario, the LHSU is heated by surrounding hot water, causing the encapsulated PCM to undergo unconstrained melting during the charging process. In this melting mode, besides thermal conduction and natural convection, the close-contact melting occurs at the bottom due to the solid PCM settling. Huang et al. [15–17] conducted comparative analyses between traditional constrained melting and close-contact melting. They reported that the presence of the close-contact melting limited the convective heat transfer to some extent, leading to the performance primarily determined by the heat conduction of the thin molten layer, and the complete melting time of the PCM in the close-contact melting mode decreased compared to that in the traditional constrained melting. Rozenfeld et al. [18] explored the close-contact melting of PCM in a horizontal double-pipe concentric storage unit with a longitudinally finned inner tube. They founded that the melting time was shortened by a factor of 2.5 compared to the case where the solid PCM was fixed. To efficiently enhance both the natural convection and the close-contact melting, our preceding research introduced an innovative wavy side wall geometry for the cylindrical LHSU, which was aimed at enhancing its thermal performance [19]. In this study, despite the notable enhancement in charging and discharging rate in comparison to the traditional cylindrical LHSU, the primary factor contributing to the enhanced discharging rate was identified as the augmentation of the heated wall surface area. Recognizing the significant impact of discharging rate on the heat output for users, there is an urgent need to enhance the heat transfer mechanism of PCM during both the charging and discharging processes. This enhancement is highly significance in optimizing the overall heat transfer efficiency of LHSUs within HWTs.

With respect to HWTs, the enclosures of the LHSU commonly take the form of a cylinder, a rectangle, and a sphere [20–22]. Among these options, the cylinder is commonly used due to its ease of manufacturing and the advantage of having a long vertical chamber that facilitates convection heat transfer [23]. For cylindrical LHSUs (C-LHSUs) within HWTs, due to the increase in the distance between the heated/cooled wall and the solid-liquid interface, the charging/discharging rate continuously decreases over time during the charging/discharging process. In particular, the charging/discharging rate significantly slows down during the final stage of these processes, resulting in longer charging/discharging times and a slower rate. Accordingly, a hollow geometry structure at the axis of the C-LHSU, which would decrease the average distance between the heated/cooled wall and the solid-liquid interface during the charging/discharging process, would be a potential strategy to enhance the thermal performance of C-LHSUs within HWTs.

Indeed, hollow geometry structures are common in tube-in-shell latent heat thermal energy storages and triple-tube latent heat storage units [24–26]. For instance, Wu et al. [27] numerically investigated the impact of toothed fins on the melting performance of PCM in a shell-and-tube latent heat storage. They reported that toothed fins have a 20 % lower fin volume than traditional circular and longitudinal fins, while has a marginally less positive impact on melting times. Kundu et al. [28] studied the effect of the inlet temperature and inlet velocity of heat fluid flow on the melting performance of PCM encapsulated in a triple-tube latent heat storage unit. The results showed that the inlet temperature has a direct impact on achieving uniform melting and lesser melting time however inlet velocity has no such effect on that due to dominant effect of free convection. In these studies, the encapsulated PCM was constrained, and thus it was statice during the melting process. Specifically, for the tube-in-shell latent heat thermal energy storage, the PCM was heated by the heat fluid flow in the inner tube, and the outer shell was assumed to be adiabatic. Accordingly, the solid PCM was constrained by the such shells during the melting process. For the triple-tube latent heat storage unit, although the PCM encapsulated in the inner annulus was heated by the heat fluid flow in the inner tube and the outer annulus, the bottom wall of the inner annulus was insulated. Accordingly, the solid PCM was also constrained by the bottom wall during the melting process. Due to such constraints, the solid PCM was static during the melting process for PCMs encapsulated in both the tube-in-shell latent heat thermal energy storage and triple-tube latent heat storage units. It is significantly different from the melting process for the PCM encapsulated within a hollow geometry C-LHSU (H-LHSU) within HWTs, where the PCM absorbs heat from the surrounding water, enabling unconstrained melting during the charging process. This disparity results in distinct melting and solidification behaviors, as well as different thermal performances.

Existing literature predominantly focuses on traditional LHSUs, with relatively limited exploration of H-LHSUs. Notably, a comprehensive analysis of the thermal performance of H-LHSUs within HWTs is currently lacking. Furthermore, compared to conventional C-LHSUs, H-LHSUs exhibit unique heat transfer mechanisms during the melting process. These distinctive characteristics may result in distinct thermal performances, yet they have not received sufficient attention. Given the critical role of PCM application in enhancing the performance of solar energy systems, further research is needed to explore practical implementation and optimization strategies to improve H-LHSUs performance.

To address these research gaps, this study will undertake innovative research in several key aspects: 1) developing an unconstrained melting model for PCM in H-LHSUs to accurately depict the unconstrained melting process in practical HWTs. This model establishment represents a novel contribution within the research domain. 2) A comprehensive thermal performance analysis of the H-LHSU will be conducted,

including melting/solidification behavior, heat transfer efficiency, and charging/discharging times. This provides a novel perspective on understanding and optimizing the impact of hollow geometry on thermal performance. 3) The impact of the ratio between the inner hollow tube radius ($r$) and outer tube radius on the charging/discharging performance of H-LHSUs will be analyzed. This analysis will offer a scientific basis for selecting the appropriate radius of the inner hollow tube in practical applications.

This study aims to fill the research gaps concerning the thermal performance of H-LHSUs within HWTs. By proposing an unconstrained melting model and employing a comprehensive analytical approach, this research provides new insights into PCM utilization in HWTs. These findings offer possibilities for future in-depth exploration and practical applications. The paper's structure is organized as follows: Section 2 presents the experimental set-up. Section 3 details the establishment of the numerical model. Section 4 presents the numerical solution and validation of the model. A comparative analysis of the thermal performances between H-LHSU and C-LHSU is provided in Section 5. Finally, Section 6 concludes the paper and outlines potential directions for future research.

## 2. Experimental set-up

An experimental set-up was designed for the unconstrained melting of PCM encapsulated within HWTs, as shown in Fig. 1. The experimental setup primarily includes the test unit, two temperature-controlled water baths, and a high-resolution camera (1920 × 1080 pixels). The test unit, with internal dimensions of 60 mm in diameter and 60 mm in height, consists of two stainless steel cylindrical heads (2 mm thick) and a transparent polycarbonate tube (2.5 mm thick). Each water bath features a square container with internal dimensions of 300 × 300 mm, enclosed by transparent polycarbonate boards (2 mm thick) on the front and rear sides. The water in the containers is heated by a 2 kW electric heater, with temperature monitored by a type T thermocouple and regulated by a temperature controller. A camera mounted on a tripod is used to record the PCM melting process.

Lauric acid, renowned for its non-toxic, biodegradable, and recyclable properties, was employed as the PCM in this study [29]. The thermophysical properties of the lauric acid, Polycarbonate, and stainless steel are outlined in Table 1. The front side material of the water bath 2 was transparent polycarbonates, and thus the camera can record the melting behavior of PCM during the melting process. The water in the water bath was heated by the electrical heater and its temperature was controlled by the temperature controller. During the testing process, the test unit was initialized in water bath 1 with a temperature of 303.15 K. Subsequently it was transferred to water bath 2, where the temperature was maintained at a temperature of 333.15 K.

## 3. Numerical model

### 3.1. Problem description and computational domain

Fig. 2 depicts schematic and computational domain of the H-LHSU and C-LHSU within HWTs. During the charging process of both H-LHSUs and C-LHSUs, heat initially traverses the enclosure before being

**Table 1**
Thermophysical properties of the materials.

| Materials | Property | value |
|---|---|---|
| Lauric acid [30] | Latent heat (kJ/kg) | 187.21 |
| | Liquids temperature (K) | 321.35 |
| | solidus temperature (K) | 316.65 |
| | Melting temperature (K) | 319 |
| | Specific heat capacity (kJ/(kg·K)) | 2.18(solid)/2.39 (liquid) |
| | Thermal conductivity (W/(m·K)) | 0.16(solid)/0.14 (liquid) |
| | Thermal expansion coefficient (1/K) | $8 \times 10^{-4}$ |
| | Density (kg/m$^3$) | 940(solid)/885(liquid) |
| | Dynamic viscosity (kg/(m·s)) | $8 \times 10^{-3}$ |
| Polycarbonate [31] | Thermal conductivity (W/(m·K)) | 0.19 |
| | Density (kg/m$^3$) | 1200 |
| | Specific heat capacity (kJ/(kg·K)) | 1.26 |
| Stainless steel [32] | Thermal conductivity (W/(m·K)) | 16.27 |
| | Density (kg/m$^3$) | 7930 |
| | Specific heat capacity (kJ/(kg·K)) | 0.5 |

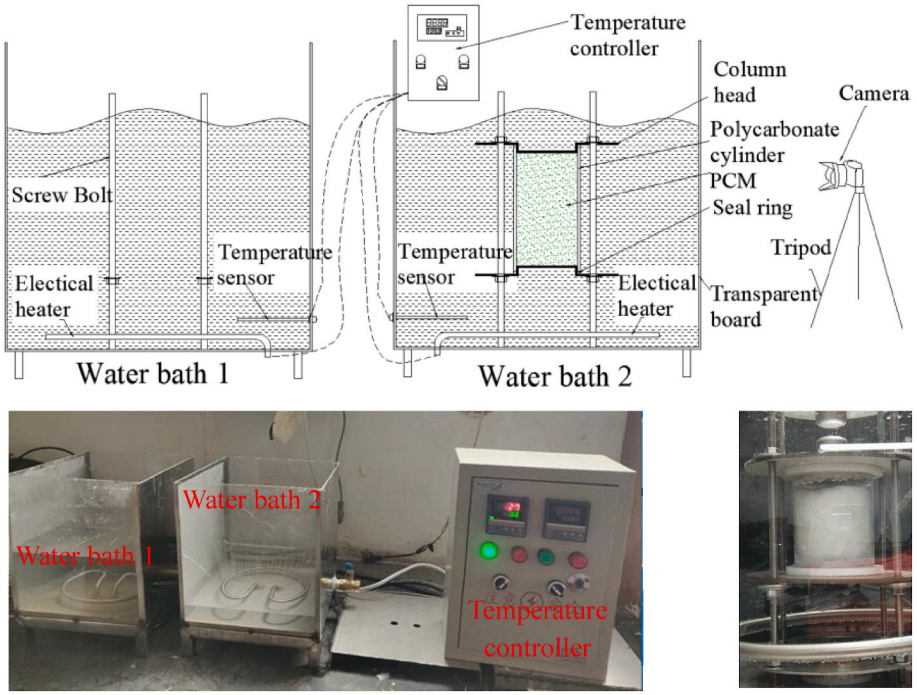


**Fig. 1.** Schematic of the experimental set-up.

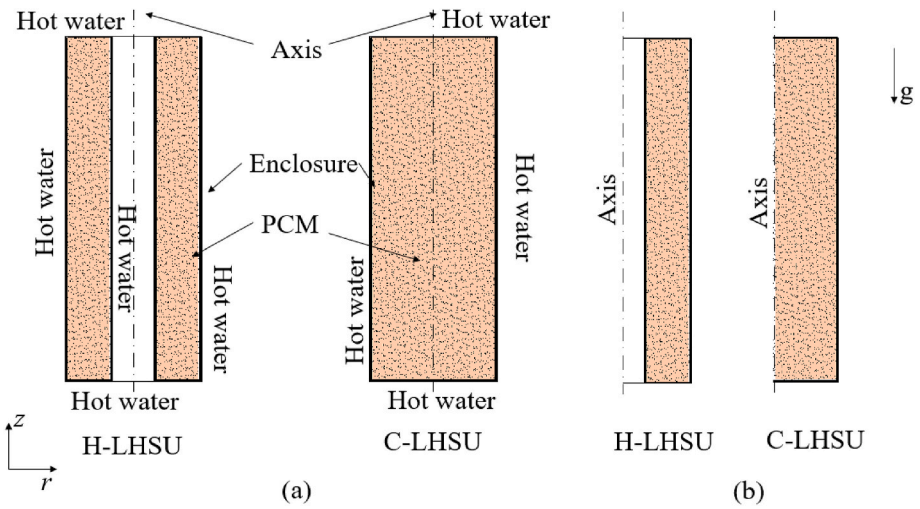


**Fig. 2.** Schematic and computational domain of the H-LHSU and the C-LHSU: (a) Schematic (b) Computational domain.

transferred to the PCM. During the discharging process, heat is transferred from the PCM to the hot water. The hot water within HWTs is assumed to remain stationary and maintain a constant temperature during both charging and discharging processes. Additionally, the PCM is assumed to possess homogeneous, isotropic, and incompressible properties [33,34]. The movement of PCMs is described as two-dimensional, laminar, and incompressible [35]. Consequently, the melting of PCM within H-LHSUs and C-LHSUs can be described using axisymmetric models. The computational domains are illustrated in Fig. 2(b). For comparative analysis, the H-LHSU and C-LHSU have been designed with identical heights. To maintain equal volumes, the outer radius of the H-LHSU is determined based on its inner hollow tube radius and the volume of the C-LHSU.

### 3.2. Mathematical model

For LHSUs placed within HWTs, unconstrained melting occurs during the charging process. To accurately model this melting behavior, the enthalpy-porosity model with a variable mushy zone constant was developed for unconstrained melting of PCM. During the discharging process, the solidification of encapsulated PCM within H-LHSUs, where the solid PCM is constrained, can be effectively modeled using the enthalpy-porosity model.

#### 3.2.1. Enthalpy-porosity model

For H-LHSUs and C-LHSUs within HWTs, the melting and solidification processes of the encapsulated PCM exhibit axisymmetric characteristics. Therefore, their heat transfer can be described by the following governing equations:

Continuity equation:

$$\frac{\partial \rho}{\partial t} + \nabla \cdot \rho V = 0 \tag{1}$$

Momentum equation:

$$\rho \frac{\partial V}{\partial t} + \rho (V \cdot \nabla) V = -\nabla p + \mu \left(\nabla^2 V\right) + \rho g \left(1 - \beta \left(T - T_{ref}\right)\right) - S \tag{2}$$

Energy equation:

$$\rho \frac{C_p \partial T}{\partial t} + \nabla \left(\rho C_p V T\right) = \nabla (\lambda \nabla T) - S_L \tag{3}$$

where, $\rho$ is represents the density, $t$ refers to the time, $V$ denotes the velocity vector, $\mu$ is the dynamic viscosity, $g$ represents the gravitational acceleration, $S$ is the Darcy source term and $S_L$ designates the energy source term.

The utilization of the Darcy source term effectively characterized the movement of the PCM in its solid and multiphase states, thus enabling the implementation of the momentum equation throughout the entire computational domain, which is specified as:

$$S = A \frac{(1-f)^2}{f^3 + \varepsilon} V \tag{4}$$

where, $A$ denotes the mushy zone constant, $\varepsilon$ represents a small computational value, $f$ stands for the liquid fraction.

The liquid fraction of a mesh element changes based on its temperature and can be determined as follows:

$$f = \begin{cases} 0 & T < T_s \\ \dfrac{T - T_s}{T_l - T_s} & T_s \le T \le T_l \\ 1 & T > T_l \end{cases} \tag{5}$$

the indices 's' and 'l' refer to solid and liquid states, respectively.

The energy source term serves to delineate the latent heat fluctuations linked with the liquid fraction of the PCM, as outlined in Ref. [36]. It can be characterized as follows:

$$S_L = \rho L \left(\frac{\partial f}{\partial t} + \nabla \cdot (V f)\right) \tag{6}$$

where, $L$ stands for the latent heat.

The thermal characteristics of the PCM undergo transitions as it shifts from the solid to the liquid state, and they can be represented as follows:

$$\rho = \rho_s + (\rho_l - \rho_s) f \tag{7}$$

$$\lambda = \lambda_s + (\lambda_l - \lambda_s) f \tag{8}$$

$$C_p = C_{p,s} + \left(C_{p,l} - C_{p,s}\right) f \tag{9}$$

#### 3.2.2. Mushy zone constant

In the enthalpy-porosity model, $A$ is utilized to depict the variation of convection velocity in relation to the liquid fraction of the PCM within the mushy zone [37]. As the magnitude of $A$ increases significantly, the movement of the solid PCM becomes fully restrained, causing its velocity to approximate zero in the model's solution [38]. Viewed from this perspective, achieving the settling velocity can be accomplished by assigning a smaller value to $A$. Consequently, accurately portraying the settling behavior would require a careful setting of the value of $A$ within the framework of the model solution.

The settling velocity, which commonly falls within the range of $10^{-4}$–$10^{-6}$ m/s as reported in Ref. [39], is relatively slow during charging processes. Due to this slow velocity, the solid PCM's settling can be approximated as quasi-steady. Accordingly, for the solid elements, Eq. (2) can be simplified in the z-direction as follows:

$$-\frac{\partial P}{\partial z}+\rho_s g\left(1-\beta\left(T-T_{ref}\right)\right)-A_s\frac{(1-f)^2}{f^3+\varepsilon}u=0 \tag{10}$$

where, $A_s$ represents the mushy zone constant for the solid element, $u$ represents the solid PCM settling velocity.

According to Bernoulli's Equation, the flow of the solid element can be described as:

$$-\frac{\partial P}{\partial z}+\rho_s u\frac{\partial u}{\partial z}+\rho_s g=0 \tag{11}$$

Given that the velocity in the solid region is equal, the value of the $\partial P/\partial z$ term is equivalent to that of the $\rho g$ term. In addition, the liquid fraction $f$ is 0 for the solid element in the solid region. Thus, Eq. (10) can be written as:

$$-\rho_s g\beta\left(T-T_{ref}\right)-\frac{A_s}{\varepsilon}u=0 \tag{12}$$

Accordingly,

$$A_s=-\frac{\rho_s g\beta\varepsilon\left(T-T_{ref}\right)}{u} \tag{13}$$

Given that the solid PCM settling velocity coincides with the liquid PCM velocity at the bottom melt front, it can be indirectly determined using the energy balance equation as follows:

$$-\lambda gradT|_{z=b}=\rho_s L u_s \tag{14}$$

Where, $gradT|_{y\,=\,b}$ denotes the temperature gradient specifically at the melt front, $b$ represents the liquid layer thickness at that location.

The liquid layer thickness at the bottom is relatively thin, hence the heat transfer within the PCM in this layer can be approximated as predominantly conductive. Accordingly, $gradT|_{y\,=\,b}$ has the same value as that of the monitored $gradT|_{y\,=\,0}$ in the model solution. Thus, $u$ is calculated as:

$$u=-\frac{\lambda gradT|_{y=0}}{\rho_s L} \tag{15}$$

Substituting Eq. (14) into Eq. (12), $A_s$ was obtained as:

$$A_s=\frac{{\rho_s}^2 Lg\,\beta\varepsilon\left(T-T_{ref}\right)}{\lambda gradT|_{y=0}+\varepsilon} \tag{16}$$

To maintain continuity within the model solution, the mushy zone constant, denoted as $A_{mu}$ in the mushy region, can be assigned a value equivalent to $A_s$ at the solidus temperature. This value is specified as follows:

$$A_{mu}=\frac{{\rho_s}^2 Lg\,\beta\varepsilon\left(T_s-T_{ref}\right)}{\lambda gradT|_{y=0}+\varepsilon} \tag{17}$$

Considering that the mushy zone constant does not affect the heat transfer properties of the PCM in its liquid state, the value assigned to the mushy zone constant is as follows:

$$A=\frac{{\rho_s}^2 Lg\,\beta\varepsilon(if(T>T_s,T_s,T)-T_m)}{\lambda gradT|_{y=0}+\varepsilon} \tag{18}$$

During the solidification process, the liquid PCM adjacent to the cooling wall surface initially solidifies into solid PCM and is constrained by the cooling wall. Accordingly, the solid PCM is static in the solidification process. To fully suppress the motion of the solid PCM, a significantly large value of $10\times10^8$ was assigned to $A$ in this study.

## 4. Numerical solution and validation

The numerical solution employed the finite element-based simulation tool, COMSOL Multiphysics, to solve the governing equations outlined above. A fully coupled approach with the direct linear solver, PARDISO, was utilized to solve the linear system of equations at each Newton-Raphson step. The time-stepping procedure adopted Euler's backward difference formula. No-slip boundary conditions were assigned to the interior wall surfaces of the enclosed domain. The boundary conditions for the numerical simulation were summarized in Table 2. The initial temperature for both the PCM and the container was 303.15K, and the initial velocity of the PCM was 0. To ensure accurate solution convergence, the tolerance factor was set to 0.001, while the relative tolerance was chosen as 0.01. Triangular meshes were utilized for discretizing the PCM domain, while quadrilateral meshes were applied to the enclosure domain. To accurately capture the physical phenomena in regions of high gradients, such as the side and bottom boundaries, the mesh was further refined in these areas. Specifically, for the bottom boundary, an eight-layer structured mesh configuration, with the first layer thickness set at 0.02 mm and a progressive growth factor of 1.2 applied to subsequent layers, was generated. For the side boundary, a three-layer structured mesh configuration, with the first layer thickness set at 0.1 mm and a progressive growth factor of 1.2 applied to subsequent layers, was generated.

Independence tests were conducted to assess the sensitivity of the solution to variations in mesh size and time step for the C-LHSU, which has a radius of 30 mm and a height of 60 mm. Three different mesh sizes were tested: 7556, 10774, and 16198 elements, respectively. The time step was initially set to 0.1 s for these tests. The findings demonstrated that the total melting time of the PCM exhibited a variance of 0.74 % between meshes comprising 7556 and 10774 elements and a deviation of 0.18 % between meshes with 10774 and 16198 elements, as shown in Fig. 3. Eventually, the mesh with 10774 elements, as shown in Fig. 4, was selected in this study.

Further investigations into the influence of the time step were conducted using the mesh with 10774 elements and time steps of 0.05, 0.1, and 0.2 s. The results demonstrated a slight disparity in the total melting time, with a 0.37 % fluctuation when comparing time steps of 0.05 s and 0.1 s, and a negligible difference between time steps of 0.1 s and 0.2 s, as shown in Fig. 5. Accordingly, a time step of 0.1s was ultimately selected.

Fig. 6 demonstrates melt fronts observed at various time intervals in the experiment and the numerical study. As evident from the comparison, the numerical melt fronts exhibited good agreement with the experimental result.

For further comparison, the experimental liquid fraction at various time intervals was calculated using edge-detection algorithms in MATLAB. Specifically, a Canny edge-detection algorithm was used to identify the location and shape of the melt front of PCM during the melting process. With the location and shape of the melt front, the volume of the solid PCM was calculated through integration. The experimental and numerical temporal evolutions of the liquid fraction are depicted in Fig. 7.

As can be seen in Fig. 7, the numerical outcomes derived from this study exhibited good agreement with the experimental findings. Further

**Table 2**
Boundary conditions for the numerical simulation.

| Boundary name | Boundary Type | Condition Description | Value/Expression |
|---|---|---|---|
| Outer wall | Isothermal wall | Constant temperature | $T$ = 333.15 K |
| Inner wall | No-Slip Wall | Zero velocity at the wall | – |
| Symmetry | Symmetry axis | Axisymmetric boundary condition | – |
| Pressure | Pressure spot | Pressure at the spot | $P$ (r = 0, z = 0) = 0 Pa |

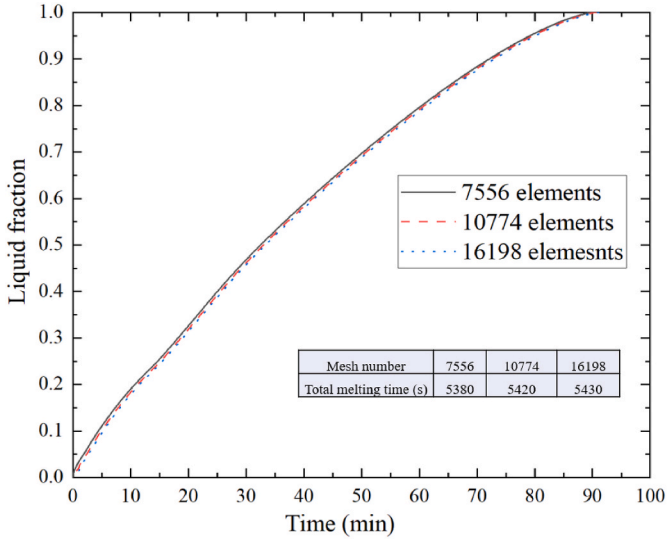


**Fig. 3.** Liquid fraction calculated with different meshes.

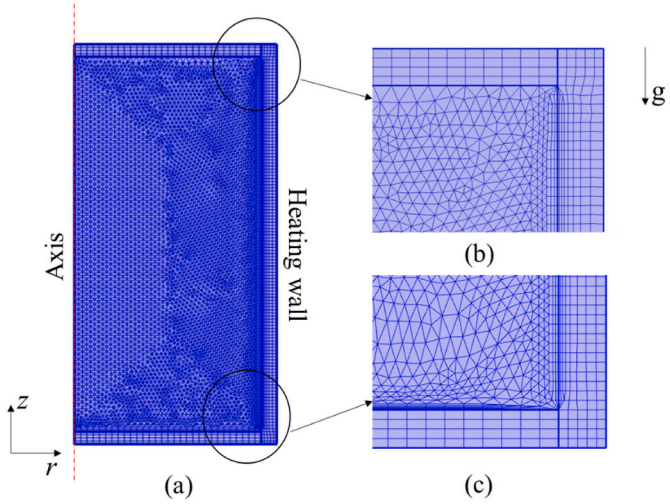


**Fig. 4.** Views of the mesh with 10774 elements: (a) Overall; (b) The magnified view at the upper right corner; (c) The magnified view at the bottom right corner.

computations demonstrate that a mean absolute relative error (MARE) of 5.2 % was achieved between the numerical results and the experimental findings. This finding shows the satisfactory precision of the model in delineating the unconstrained melting process of PCM within H-LHSUs.

## 5. Results and discussion

### 5.1. Thermal performance of H-LHSU vs. C-LHSU

In this section, a comparative analysis was conducted between the H-LHSU and C-LHSU in terms of melting/solidification behavior, heat transfer efficiency, and charging/discharging times. The height and the inner radius of the C-LHSU were 300 mm and 30 mm, respectively. Meanwhile, the H-LHSU shared the same height as the cylindrical LHSU but featured an inner hollow tube radius of 10 mm. To maintain parity in volume with the C-LHSU, the outer radius of the H-LHSU was adjusted to 31.6 mm. Both types of LHSUs feature a stainless-steel enclosure with a thickness of 1 mm. During the charging process, the LHSUs were initially set at a temperature of 303.15 K, while the water in HWTs was

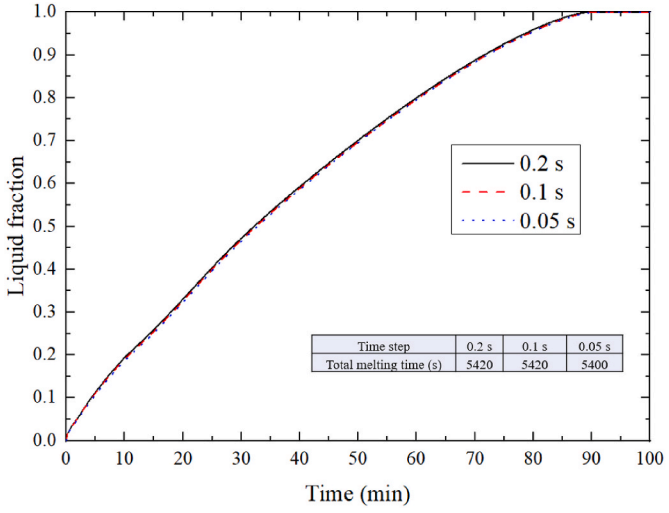


**Fig. 5.** Liquid fraction calculated with different time steps.

maintained at 333.15 K. Conversely, the LHSUs were initially set at 333.15 K, and the water temperature in the tanks was set to 303.15 K in the discharging process.

#### 5.1.1. Charging process

Fig. 8 illustrates temperature distributions of the H-LHSU and C-LHSU during the charging process. In the figures, velocity vectors of the liquid-phase PCM are denoted by black arrows, while the solid-liquid interface of the PCM is represented by a black line.

During the initial phase, hot water was employed to heat the LHSUs, resulting in a rapid temperature increase of the PCM adjacent to the enclosure and the subsequent formation of a thin liquid layer, as depicted in the temperature contour plot at 1 min. Due to the limited thickness of this liquid layer, a relatively larger viscous force exists between the solid surface and the enclosure's inner surface, resulting in the relatively state of the liquid PCM. Therefore, thermal conduction emerges as the dominant heat transfer mechanism within the PCM during this early phase. As time progresses, the liquid layer gradually thickens, and natural convection occurs as the buoyancy force of the liquid PCM eventually overcomes the viscous resistance offered by the enclosure wall, as depicted in the temperature contour plot at 10 min. It should be mentioned that the solid PCM was surrounded by the liquid PCM. Due to the gravitational force, the solid PCM dropped slowly and exerted a pressure on the underlying liquid PCM. Under this pressure, the bottom liquid PCM flowed outward along the radial direction and then pushed the side liquid PCM upward along the heated side wall, resulting in a thin liquid PCM layer at the bottom. Consequently, a thin layer of liquid PCM formed at the bottom, facilitating contact melting in this region. Compared to the C-LHSU, the solid PCM encapsulated in the H-LHSU exhibited a higher average temperature. Two factors could explain this observation. Firstly, heat is transferred through the outer wall surface of the C-LHSU, but in the H-LHSU, it can be transferred through both the inner and outer tube wall surfaces. Accordingly, compared to the C-LHSU, the area of the heated wall surface area is larger in the H-LHSU. Secondly, the distance between the heated wall surface and the encapsulated PCM in the H-LHSU was smaller compared to the C-LHSU, and thus the thermal resistance was lower. This indicates that the H-LHSU offers superior thermal conductivity. After heating the LHSUs for 30 min, a curved surface was observed on the solid PCM. This phenomenon can be explained by the descent of the liquid PCM along the solid-liquid interface, followed by the establishment of natural convection currents within the liquid regions. Since the H-LHSU was heated by both its outer and inner tube wall surfaces, natural convection occurred near such surfaces. Given that convection circulation, induced

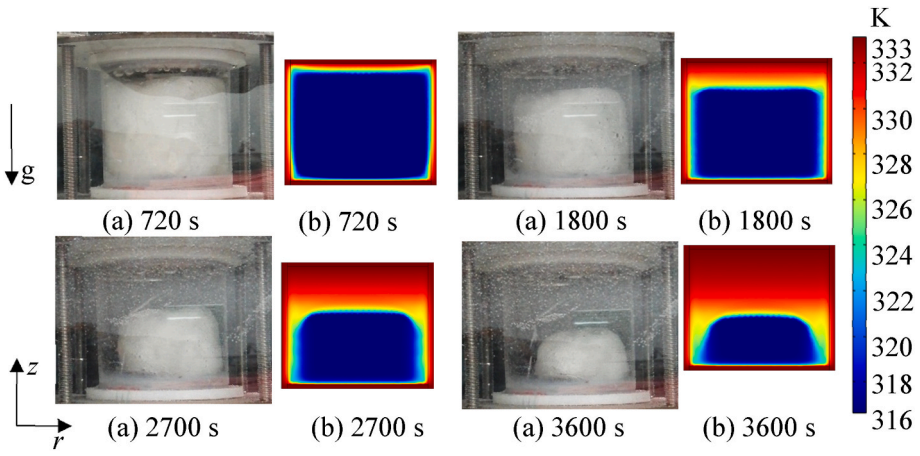


**Fig. 6.** Melt fronts observed at various time intervals: (a) experimental; (b) numerical.

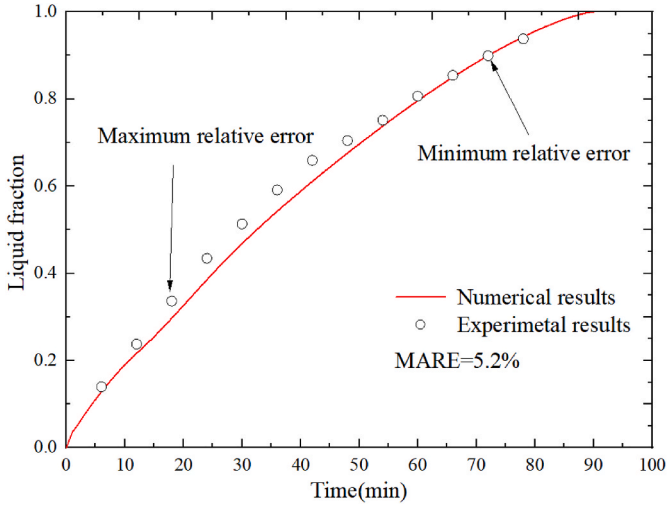


**Fig. 7.** Experimental and numerical temporal evolution of the liquid fraction.

by natural convection, efficiently transfers heat from the heated wall to the solid PCM, the natural convection of the PCM within the H-LHSU is expected to be improved compared to that within the C-LHSU. Furthermore, the decreased distance between the heated wall surface and the solid PCM in the H-LHSU leads to a shorter convection circulation pathway for the PCM. This would facilitate a more rapid transfer of heat from the hot water to the PCM. As time progresses to 63 min, the solid PCM within the H-LHSU has fully melted, whereas a substantial quantity of solid PCM still remains in the C-LHSU.

To further investigate the heat transfer performances of the H-LHSU and C-LHSU during the charging process, Fig. 9 illustrates the variations of heat transfer coefficients at the heated wall surface. Due to thermal stratification, heat transfer within the liquid PCMs in the upper region is primarily governed by conduction. Accordingly, this study does not provide insights into the fluctuations of the heat transfer coefficients specifically at the top heated wall.

As observed in Fig. 9(a), during the initial phase, where conduction is the dominant mode of heat transfer, the transient heat transfer coefficients were nearly identical for both the H-LHSU and C-LHSU. As time progressed, natural convection came into play, and the heat transfer began to be influenced by a combination of conduction and convection. Due to the improvement of both conduction and natural convection heat transfer for the H-LHSU, the transient heat transfer coefficient at the side surface exceeded that of the C-LHSU. Subsequently, the transient heat transfer coefficient for the H-LHSU decreased to a value lower than that of the C-LHSU. This reduction can primarily be attributed to the ongoing melting of solid PCM in the H-LHSU, which led to a larger volume of liquid PCM and consequently, an increase in thermal resistance. As the solid PCM completely melts, the transient heat transfer coefficient sharply decreased to a minimum value. Regarding the bottom, the transient heat transfer coefficient of the H-LHSU tended to be lower than that of the C-LHSU, as depicted in Fig. 9(b). This result

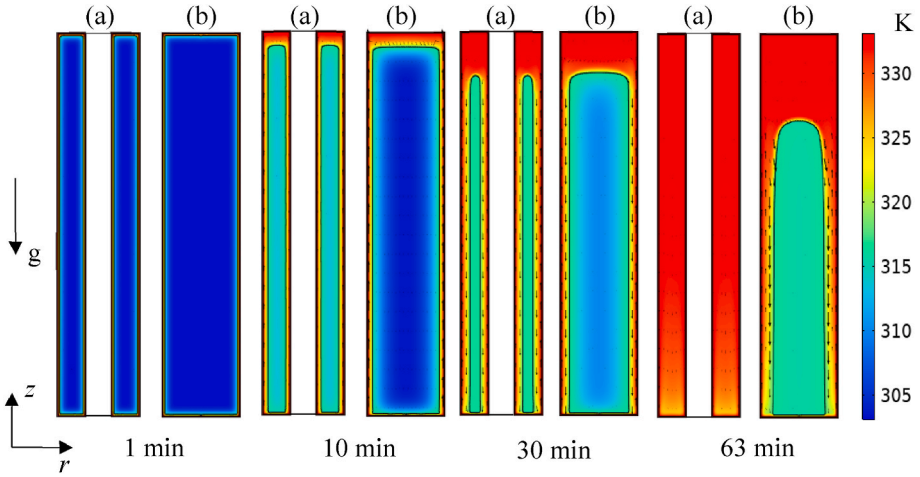


**Fig. 8.** Temperature distribution within the LHSUs during the charging process: (a) H-LHSU; (b) C-LHSU.

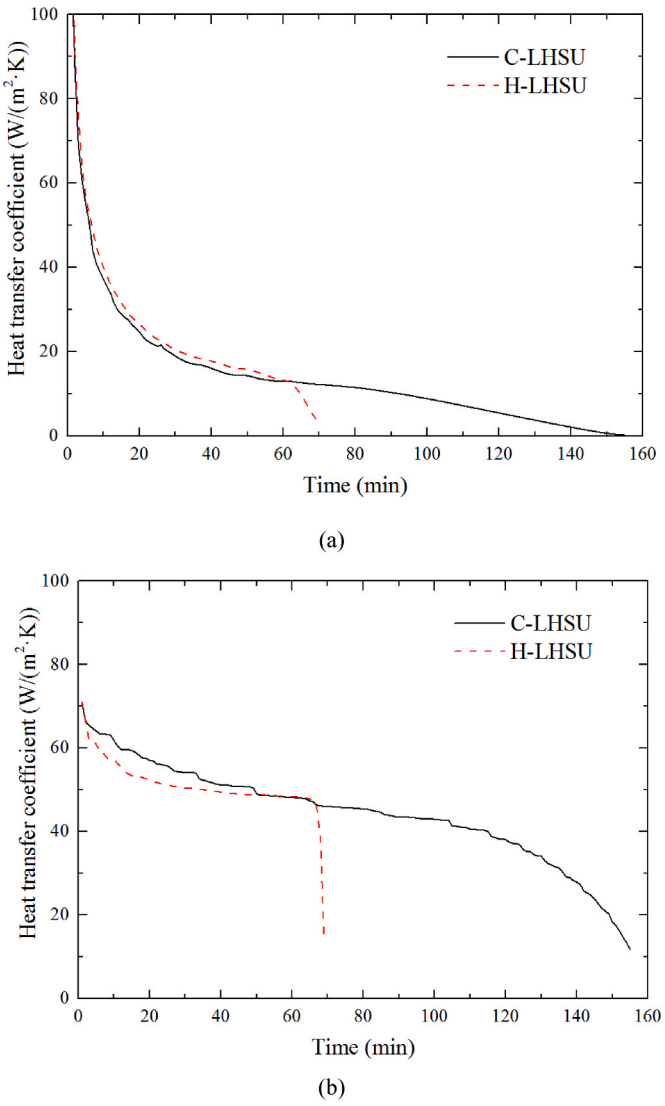


**Fig. 9.** Variations of heat transfer coefficients at the heated wall surface during the charging process: (a) side; (b) bottom.

can be explained by the fact that the melt rate of the solid PCM within H-LHSU is larger than that of the C-LHSU. Accordingly, compared to the C-LHSU, the H-LHSU has a smaller contact area between the solid PCM and the bottom heated wall surface, leading to a decrease in the intensity of the close-contact melting.

To enable a more extensive comparison, the average heat transfer coefficients were calculated for both the H-LHSU and C-LHSU, and the findings are summarized in Table 3.

As presented in Table 3, the average heat transfer coefficient at the side wall of the C-LHSU was 14.39 W/(m$^2$·K), whereas for the H-LHSU it was 26.32 W/(m$^2$·K). This indicates an increase of 82.9 % for the H-LHSU compared to the C-LHSU. This finding indicates a significant enhancement in the heat transfer of the side wall surface during the charging process for the H-LHSU compared to the C-LHSU. Regarding the bottom heated wall, despite having a smaller transient heat transfer coefficient than the C-LHSU, the H-LHSU exhibited a slightly higher average heat transfer coefficient. This can be attributed to the notably shorter charging time of the H-LHSU, which was considered in the calculation of its average heat transfer coefficient relative to that of the C-LHSU. Specifically, the average heat transfer coefficient of the C-LHSU was 42.37 W/(m$^2$·K), while that of the H-LHSU was 50.47 W/(m$^2$·K). Compared to the C-LHSU, the H-LHSU demonstrated a 19.12 % increase in the average heat transfer coefficient. Therefore, it can be concluded that the hollow geometry effectively enhances heat transfer at the bottom heated wall surface of the H-LHSU during the charging process.

**Table 3**
Average heat transfer coefficients during the charging process.

| Wall surface | C-LHSU | | H-LHSU | |
|---|---|---|---|---|
| | Side wall | Bottom wall | Side wall | Bottom wall |
| Average heat transfer coefficient (W/(m$^2$·K)) | 14.39 | 42.37 | 26.31 | 50.47 |

The temporal evolution of the PCM's liquid fraction during the charging process for both the C-LHSU and H-LHSU is depicted in Fig. 10. Notably, the curve representing the H-LHSU's liquid PCM lies to the left of the C-LHSU's curve, signifying a faster melting rate of the PCM within the H-LHSU. This enhanced melting rate can be attributed to the improved heat transfer in the H-LHSU compared to the C-LHSU. Further analysis reveals that the charging times for the H-LHSU and C-LHSU are 63 and 155 min, respectively. This translates to a charging rate for the H-LHSU that is 2.46 times faster than that of the C-LHSU. It should be mentioned that in our previous study [19], the charging rate of the PCM encapsulated in the C-LHSU with a wavy side wall was 2.42 times that in the C-LHSU with straight side wall. This indicates that, for the C-LHSU, the hollow geometry exhibits nearly identical enhancement in the charging rate compared to the wavy side wall design during the charging process. Consequently, the hollow geometry can significantly enhance the charging rate of the C-LHSU.

### 5.1.2. *Discharging process*

Fig. 11 illustrates temperature distributions of both the H-LHSU and C-LHSU during the discharging process. In these figures, velocity vectors of the liquid-phase PCM are denoted by black arrows, while the solid-liquid interface of the PCM is represented by a black line.

In the initial stages, the LHSUs were subjected to cooling by the surrounding hot water within the HWTs, resulting in a rapid drop in temperature of the PCM adjacent to the cooled wall surfaces. This PCM then descended along the cooled wall surface, giving rise to natural convection within the liquid PCM, as evident from the temperature cloud diagram captured at 1 min. Similar to the charging process, convective circulations of the liquid PCM formed in close proximity to both the outer and inner cooled walls. Consequently, a greater number of convection circulations were observed compared to the C-LHSU, indicating that the natural convection occurring within the H-LHSU is

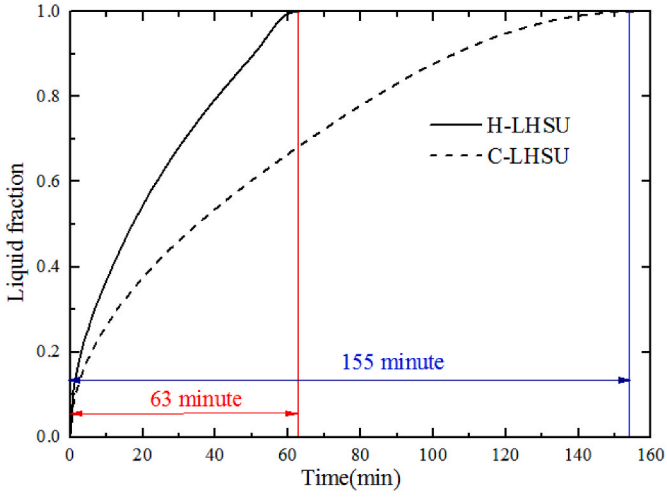


**Fig. 10.** Temporal evolution of the liquid fraction of the PCM during the charging process for the C-LHSU and H-LHSU.

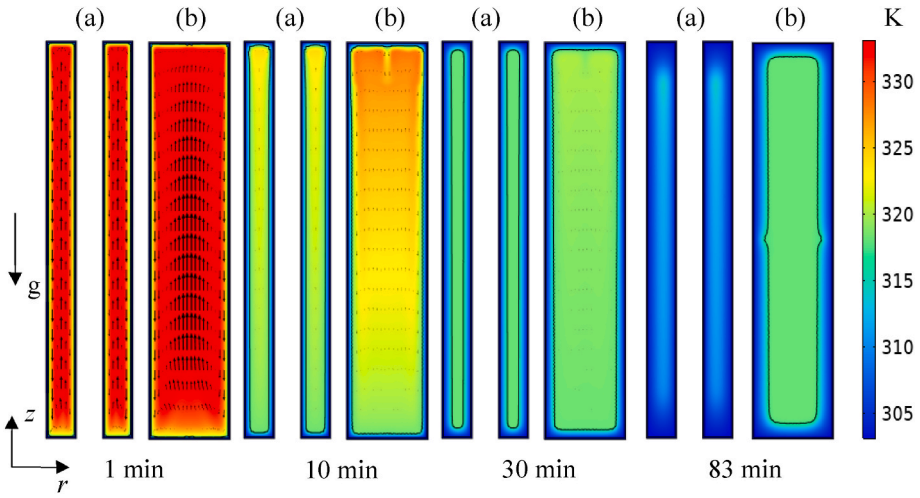


**Fig. 11.** Temperature distribution within the LHSUs the discharging process: (a) H-LHSU; (b) C-LHSU.

more pronounced than that of the C-LHSU. Over time, the temperature of the PCM decreased, reducing temperature differences acrross various locations. Consequently, the intensity of natural convection diminished, as shown in the temperature cloud diagram at 10 min. It is worth highlighting that the average temperature of the PCM was lower for the H-LHSU compared to the C-LHSU, indicating that the H-LHSU demonstrates superior thermal conductivity compared to the C-LHSU. As the duration progressed to 30 min, the temperature differences at various locations became relatively insignificant, making natural convection negligible. This indicates that thermal conduction would predominate as the primary mechanism for heat transfer. Similar to the charging process, the average gap between the cooled wall surface and the encapsulated PCM is narrower in the H-LHSU than in the C-LHSU. This leads to higher thermal conductivity for the H-LHSU compared to the C-LHSU. Consequently, the PCM encapsulated within the H-LHSU solidifies at a faster rate than that within the C-LHSU. When the LHSUs were cooled for 83 min, the liquid PCM within the H-LHSU had already completely solidified, while the PCM in the C-LHSU remained liquid.

To provide a more comprehensive comparison of the heat transfer performances between the C-LHSU and H-LHSU, Fig. 12 illustrates the fluctuations in the heat transfer coefficients during the discharging process.

As evident from Fig. 12(a), the transient heat transfer coefficient at the side wall surface of the H-LHSU initially surpassed that of the C-LHSU. This observation can be attributed to the enhanced thermal conduction and natural convection of the PCM encapsulated within the H-LHSU in comparison to the C-LHSU. Subsequently, it exhibited a tendency to become smaller than that of the C-LHSU. Similarly, for the bottom wall, as depicted in Fig. 12(b), it was initially higher but later tended to decrease in comparison to that of the C-LHSU.

To enable a more extensive comparison, the average heat transfer coefficients were calculated for both the H-LHSU and C-LHSU, and the findings are summarized in Table 4.

As presented in Table 4, the average heat transfer coefficient at the side wall of the C-LHSU during the discharging process was 5.61 W/($m^2$·K), whereas for the H-LHSU, it notably increased to 15.51 W/($m^2$·K). This represents an increase of 176.47 % for the H-LHSU compared to the C-LHSU, highlighting a substantial improvement in heat transfer. Regarding the bottom wall, it was 1.77 W/($m^2$·K) for the C-LHSU, while for the H-LHSU, it was 3.84 W/($m^2$·K). This indicates an increase of 116.95 % for the H-LHSU compared to the C-LHSU, further emphasizing the significant enhancement in heat transfer at the bottom wall for the H-LHSU. In summary, the data presented in Table 4 clearly demonstrates that the heat transfer performance of both the side and bottom wall surfaces during the discharging process was significantly

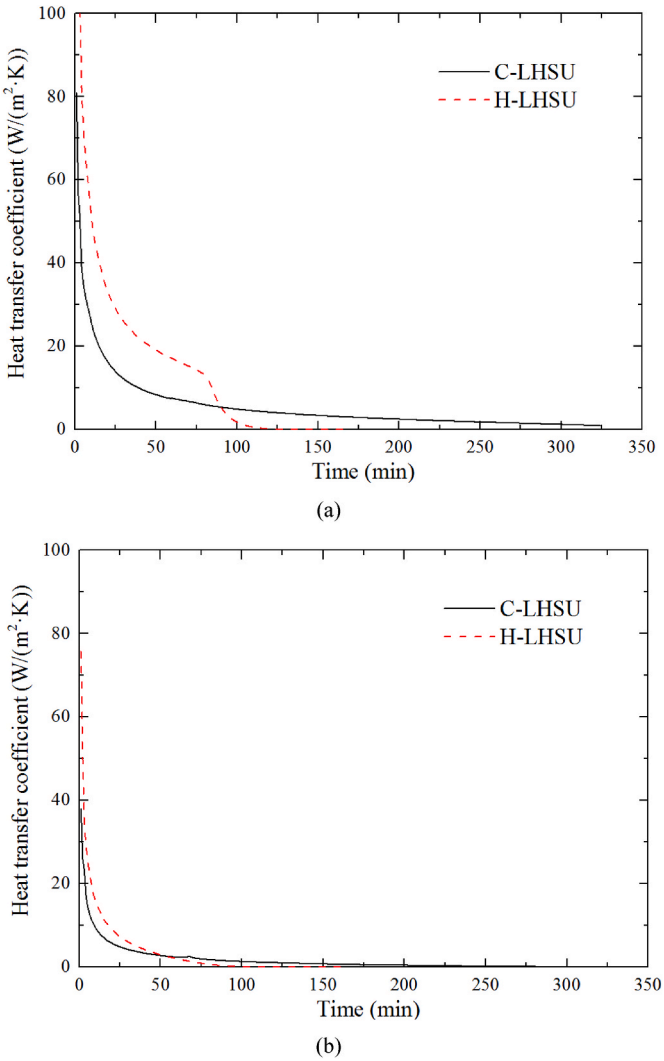


**Fig. 12.** Changes in heat transfer coefficients during the discharging process: (a) side; (b) bottom.

improved in the H-LHSU compared to the C-LHSU.

Fig. 13 shows the temporal evolution of the PCM's fraction during the discharging process of the C-LHSU and H-LHSU. It is evident that

**Table 4**
Average heat transfer coefficients during the discharging process.

| Wall surface | C-LHSU | | H-LHSU | |
|---|---|---|---|---|
| | Side wall | Bottom wall | Side wall | Bottom wall |
| Average heat transfer coefficient ($W/(m^2 \cdot K)$) | 5.61 | 1.77 | 15.51 | 3.84 |

when compared to the C-LHSU, the H-LHSU exhibited a steeper slope on the curve. More precisely, the discharging process for the H-LHSU took 83 min, whereas for the C-LHSU it lasted 324 min. This discrepancy implies that the discharging rate of the H-LHSU was approximately 3.9 times faster than that of the C-LHSU. It should be mentioned that in our preceding research [19], the discharging rate of the PCM encapsulated in the C-LHSU with a wavy side wall was 1.47 times that in the C-LHSU with straight side wall. Notably, the hollow geometry design demonstrates significantly greater enhancement in the discharging rate compared to the wavy side wall design during the discharging process. Therefore, the hollow geometry design could be an effective approach to improving the discharging rate of C-LHSUs.

### 5.2. Effect of r/R on the thermal performance of H-LHSUs

In this section, the effect of the ratio between the inner and outer tube radius on the charging/discharging performance of H-LHSUs was analyzed. All of the H-LHSUs had the same volume of 0.848 L and shared the same height of 300 mm. Given that the thermal conductivity of stainless steel significantly exceeds that of the PCM, the thickness of the enclosure in such H-LHSUs was neglected during the charging and discharging process of the encapsulated PCM. The ratios of the inner tube radius ($r$) to the outer tube radius ($R$) for the H-LHSUs were chosen with values of 0.1, 0.2, 0.3, 0.4 and 0.5, and the corresponding inner and outer tube radius were calculated and presented in Table 5.

#### 5.2.1. Charging performance

Fig. 14 depicts the variation of liquid fraction during the charging process for H-LHSUs with different $r/R$. As can be seen, the profile of Liquid fraction-Time shifted to left as $r/R$ increased from 0.1 to 0.5. This shift signifies an acceleration in the melting rate of the encapsulated PCM as the $r/R$ increases. Table 6 illustrates the charging time of PCM encapsulated in H-LHSUs. To facilitates analysis, the total surface area of the H-LHSUs with different $r/R$ was also presented. As can be seen, the charging time decreased with the increased of $r/R$. Specifically, as $r/R$ increased from 0.1 to 0.5, the charging time decreased from 96 to 46 min, indicating an increase in the charging rate by 108.7 %. This result can be explained by the fact that as $r/R$ increased from 0.1 to 0.5, the total heated wall surface of the H-LHSU increased from $6.81 \times 10^{-2}$ to $10.35 \times 10^{-2}$ $m^2$, with an increase of 51.98 %. Additionally, both the thermal conduction and nature convection of PCMs within the LHSU was enhanced with the increase of $r/R$.

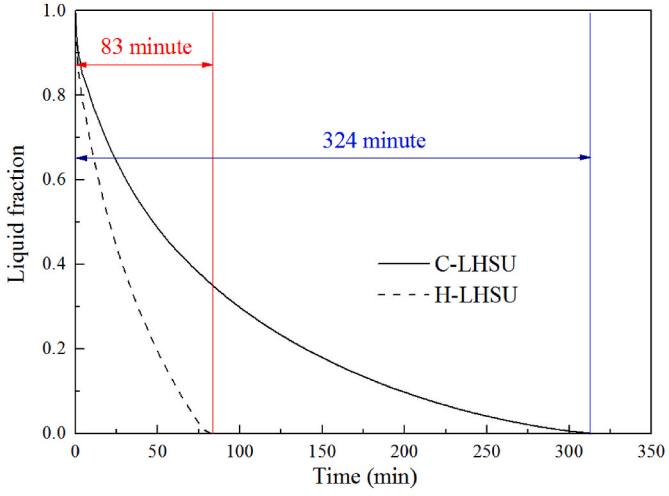


**Fig. 13.** Temporal evolution of the liquid fraction of the PCM during the discharging process.

**Table 5**
Dimension of H-LHSUs with different $r/R$.

| $r/R$ | Inner tube radius (mm) | Outer tube radius (mm) | Height (mm) |
|---|---|---|---|
| 0.1 | 3.015 | 30.15 | 300 |
| 0.2 | 6.12 | 30.62 | 300 |
| 0.3 | 9.43 | 31.45 | 300 |
| 0.4 | 13.09 | 32.73 | 300 |
| 0.5 | 17.32 | 34.64 | 300 |

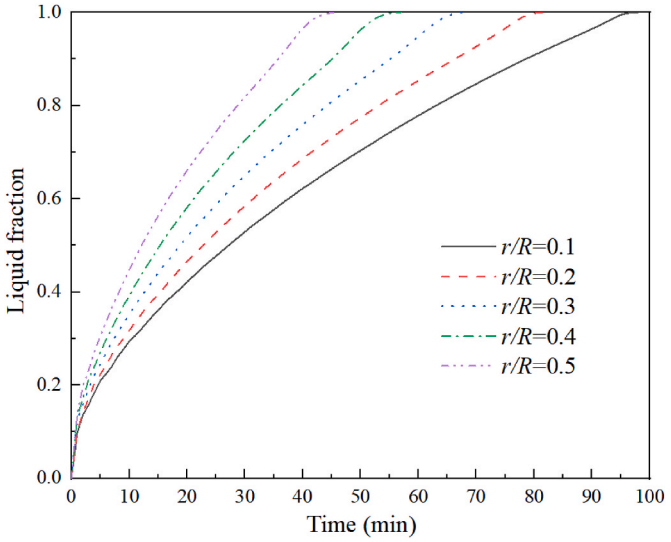


**Fig. 14.** Temporal evolution of the liquid fraction during the charging process for H-LHSUs with different $r/R$.

**Table 6**
The charging time of H-LHSUs with different $r/R$.

| $r/R$ | 0.1 | 0.2 | 0.3 | 0.4 | 0.5 |
|---|---|---|---|---|---|
| Charging time (min) | 96 | 82 | 69 | 57 | 46 |
| Total surface area ($m^2$) | $6.81 \times 10^{-2}$ | $7.49 \times 10^{-2}$ | $8.27 \times 10^{-2}$ | $9.20 \times 10^{-2}$ | $10.35 \times 10^{-2}$ |

To conduct a more in-depth analysis, the increase in the charging rate of H-LHSUs was calculated when $r/R$ increased by 0.1, as presented in Table 6. In addition, the corresponding increase in the total heated wall surface was also presented. Given that the charging rate of the H-LHSU increases proportionally with both the heated wall surface area and the heat transfer coefficient, the increase in average heat transfer coefficient can be calculated by dividing the enhancement factor of the charging rate by the enhancement factor of the heated wall surface area. Specifically, this is calculated as (1+increase in charging rate) divided by (1+increase in total surface area). To facilitate the analysis, the average heat transfer coefficient between the hot water and PCM within the H-LHSUs was calculated and presented in Table 7.

As observed, for each increment of 0.1 in $r/R$, there was a corresponding increase in both the charging rate and the average heat transfer coefficient. Notably, this increase in value became more significant as $r/R$ increased. This suggests that for a given increment in $r/R$,

**Table 7**
The increase in performance parameters of H-LHSUs with the increase of *r/R*.

| Parameters | *r/R* | | | |
|---|---|---|---|---|
| | 0.1 to 0.2 | 0.2 to 0.3 | 0.3 to 0.4 | 0.3 to 0.5 |
| Charging rate | 17.07 % | 18.84 % | 21.05 % | 23.91 % |
| Total heated wall surface area | 9.99 % | 10.41 % | 11.25 % | 12.50 % |
| Average heat transfer coefficient | 6.44 % | 7.63 % | 8.82 % | 10.14 % |

the enhancement in heat transfer of PCM encapsulated in H-LHSUs becomes more significant as *r/R* rises during the charging process. It should be mentioned that the expansion in the total heated wall surface also intensifies with an increase in *r/R*, which subsequently leads to an increase in the capital cost of the H-LHSU. Accordingly, a careful trade-off between the required charging rate and the capital cost of the H-LHSU should be made when selecting the appropriate *r/R* for practical applications.

### 5.2.2. Discharging performance

Fig. 15 depicts the variation of liquid fraction during the discharging process for H-LHSUs with different *r/R*. Similar to the charging process, the profile of Liquid fraction-Time shifted to left as *r/R* increased from 0.1 to 0.5. This shift indicates an acceleration in the solidification rate of the encapsulated PCM as the *r/R* increases. Table 8 illustrates the discharging time of PCM encapsulated in H-LHSUs. To facilitates analysis, the total surface area of the H-LHSUs with different *r/R* was also presented. As can be seen, the discharging time decreased with the increased of *r/R*. Specifically, as *r/R* increased from 0.1 to 0.5, the discharging time decreased from 150 to 55 min, indicating an increase in the discharging rate by 167.27 %. Two factors could explain this observation. Firstly, as *r/R* increased from 0.1 to 0.5, the total heated wall surface of the H-LHSU increased from $6.81 \times 10^{-2}$ to $10.35 \times 10^{-2}$ $m^2$, with an increase of 51.98 %. Secondly, the thickness between the inner tube and outer tube of the H-LHSU decreased with the increase of *r/R*, leading to the decrease in the average distance between the cooled wall surface and the PCM. Accordingly, the thermal resistance during the discharging process of the H-LHSU would decrease with the increase of *r/R*.

For further analysis, the increase in the discharging rate of H-LHSUs was calculated when *r/R* increased by 0.1, as presented in Table 9. Similar to the charging process, the increase in the total cooled wall surface area and the average heat transfer coefficient between the hot

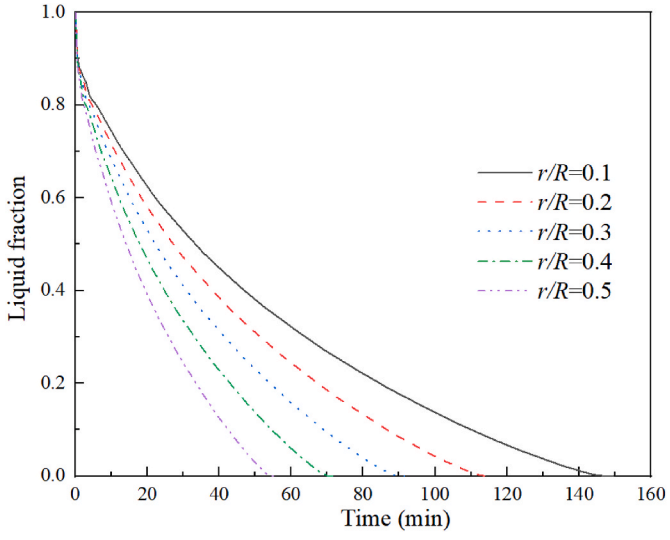


**Fig. 15.** Temporal evolution of the liquid fraction during the discharging process for H-LHSUs with different r/R.

**Table 8**
The discharging time of H-LHSUs with different *r/R*.

| *r/R* | 0.1 | 0.2 | 0.3 | 0.4 | 0.5 |
|---|---|---|---|---|---|
| Discharging time (min) | 147 | 117 | 92.5 | 72 | 55 |
| Total surface area ($m^2$) | $6.81 \times 10^{-2}$ | $7.49 \times 10^{-2}$ | $8.27 \times 10^{-2}$ | $9.20 \times 10^{-2}$ | $10.35 \times 10^{-2}$ |

water and PCM within the H-LHSUs during the discharging process were also calculated.

Similar to the charging process, the discharging rate and the average heat transfer coefficient of H-LHSUs both demonstrated a concurrent increase in response to the elevation of *r/R*. Specifically, for each increment of 0.1 in *r/R*, there was a notably more significant increase in the value of this increase. Accordingly, as *r/R* increases during the discharging process, the enhancement in heat transfer of PCM encapsulated in H-LHSUs also becomes more significant for a given increment in *r/R*. Similarly, due to the increase in the total surface area of the H-LHSUs as *r/R* increases, a careful trade-off between the required discharging rate and the capital cost of the H-LHSU also should be made when selecting the appropriate *r/R* for practical applications.

## 6. Conclusions and future studies

In this study, a comprehensive analysis of the charging/discharging performance of PCM encapsulated within the H-LHSU inside HWTs was conducted. Initially, an unconstrained melting model for the PCM encapsulated in H-LHSUs was developed, verified for accuracy, and subsequently utilized to simulate both the melting and solidification processes. The outcomes, encompassing melting/solidification behavior, heat transfer coefficients, and charging/discharging time, were analyzed and compared to those observed in the C-LHSU. To facilitate the selection radius of the inner hollow tube, the impact of *r/R* on the charging/discharging performance of H-LHSUs was analyzed. The principal discoveries of this study are summarized as follows.

- The hollow geometry design of the C-LHSU significantly enhanced thermal conduction and natural convection at the side heated wall surface. Specifically, the average heat transfer coefficients at this surface increased by 82.9 % during charging and 176.47 % during discharging compared to the C-LHSU.
- The hollow geometry design significantly enhanced the charging and discharging rates of the C-LHSU. Specifically, the H-LHSU exhibited a 2.46 times faster charging rate and a 3.9 times quicker discharging rate compared to the C-LHSU.
- Both the charging and discharging rates of the H-LHSU increased with *r/R*. Specifically, as *r/R* increased from 0.1 to 0.5, the charging and discharging rate rose by 108.7 % and 167.27 %, respectively.
- As *r/R* increases, the heat transfer enhancement of PCM in H-LHSUs becomes more significant during both the charging and discharging process. When selecting *r/R* for the H-LHSU, A careful trade-off between the charging rate and capital cost is essential in practical applications.

This study conclusively establishes that the H-LHSU outperforms the

**Table 9**
The increase in performance parameters of H-LHSUs with the increase of *r/R*.

| Parameters | *r/R* | | | |
|---|---|---|---|---|
| | 0.1 to 0.2 | 0.2 to 0.3 | 0.3 to 0.4 | 0.3 to 0.5 |
| Discharging rate | 25.64 % | 26.49 % | 28.47 % | 30.91 % |
| Total cooled wall surface area | 9.99 % | 10.41 % | 11.25 % | 12.50 % |
| Average heat transfer coefficient | 14.23 % | 14.56 % | 15.48 % | 16.36 % |

C-LHSU in terms of thermal performance during both charging and discharging processes, positioning it as a promising option for enhancing the thermal efficiency of C-LHSU in HWTs. Future endeavors will focus on integrating H-LHSU into HWTs to elevate their overall thermal performance. Furthermore, considering the significant effects of PCM properties, thermal boundary conditions, and geometric parameters on charging and discharging durations, a comprehensive parametric analysis is planned. Additionally, to facilitate the practical implementation of H-LHSU, design aids will be developed in the future studies.

## CRediT authorship contribution statement

**Zhongjun Yan:** Writing – original draft, Methodology, Investigation, Funding acquisition, Formal analysis, Data curation, Conceptualization. **Zhengxuan Liu:** Writing – review & editing, Writing – original draft, Supervision, Software, Methodology, Investigation, Formal analysis, Conceptualization. **Yongqiang Luo:** Writing – review & editing, Methodology, Investigation. **Shulin Pan:** Writing – original draft, Methodology, Investigation. **Wang Chen:** Writing – original draft, Methodology, Investigation. **Yuan Zhang:** Writing – original draft, Methodology, Investigation. **Ke Liang:** Writing – original draft, Methodology, Investigation.

## Declaration of competing interest

The authors declare that they have no known competing financial interests or personal relationships that could have appeared to influence the work reported in this paper.

## Acknowledgement

The authors express their heartfelt appreciation for the generous support provided by the Outstanding Youth Program of the Hunan Provincial Department of Education (No.23B0812), Hunan Provincial Natural Science Foundation of China (No.2023JJ50478, No.2024JJ7260, No.2025JJ70303) and the Hunan Provincial Innovation Foundation for Postgraduate (No.CX20231268).

## Data availability

Data will be made available on request.

## References

[1] Da Col A, et al. Modelling a latent heat thermal storage demonstrator and identification of the model key-parameters. J Energy Storage 2023;73:109239.
[2] Belmonte JF, et al. Simulated performance of a solar-assisted heat pump system including a phase-change storage tank for residential heating applications: a case study in Madrid, Spain. J Energy Storage 2022;47:103615.
[3] Xu Q, et al. Heat transfer enhancement performance of microencapsulated phase change materials latent functional thermal fluid in solid/liquid phase transition regions. Int J Heat Mass Tran 2023;214:124461.
[4] Triki R, Chtourou S, Baccar M. Heat transfer enhancement of phase change materials PCMs using innovative fractal H-shaped fin configurations. J Energy Storage 2023;73:109020.
[5] Zhu X, et al. Geometry-induced thermal storage enhancement of shape-stabilized phase change materials based on oriented carbon nanotubes. Appl Energy 2019;254:113688.
[6] Aissa A, et al. Enhanced heat transmission in a triangular enclosure with a rotating cooled wall using Nano-Encapsulated Phase Change Material nanofluid under mixed convection. Case Stud Therm Eng 2024;54:103992.
[7] Ranjan R, Kumar R, Srinivas T. Thermal performance of nano-enhanced phase change material and air-based lithium-ion battery thermal management system: an experimental investigation. J Energy Storage 2024;82:110567.
[8] Najafpour N, Adibi O. Investigating the effects of nano-enhanced phase change material on melting performance of LHTES with novel perforated hybrid stair fins. Energy 2024;290:130232.
[9] Zare P, et al. A novel thermal management system for cylindrical lithium-ion batteries using internal-external fin-enhanced phase change material. Appl Therm Eng 2024;238:121985.
[10] Shen S, et al. Investigation on latent heat energy storage using phase change material enhanced by gradient-porosity metal foam. Appl Therm Eng 2024;236:121760.
[11] Qahiti R, Almarashi A, Hamali W. Thermal behavior of nanoparticle enhanced phase change material discharging in existence of complex geometry. J Energy Storage 2023;59:106450.
[12] El Mghari H, et al. Selection of phase change materials, metal foams and geometries for improving metal hydride performance. Int J Hydrogen Energy 2020;45(29):14922–39.
[13] Dhaidan NS, et al. Experimental and numerical investigation of melting of NePCM inside an annular container under a constant heat flux including the effect of eccentricity. Int J Heat Mass Tran 2013;67:455–68.
[14] Seddegh S, et al. Comparison of heat transfer between cylindrical and conical vertical shell-and-tube latent heat thermal energy storage systems. Appl Therm Eng 2018;130:1349–62.
[15] Huang Y, Huang P, Yu C. Close-contact melting enhancement mechanisms in space-constrained and large-space containers. Int J Heat Mass Tran 2025:237.
[16] Huang Y, Zhai H, Deng Z. A novel elastic-driven phase-change thermal buffer for efficient thermal management. Int J Heat Mass Tran 2025:239.
[17] Huang Y, et al. Gravity-driven close contact melting heat transfer in gradient latent heat storage units. Int Commun Heat Mass Tran 2024;156.
[18] Rozenfeld T, et al. Close-contact melting in a horizontal cylindrical enclosure with longitudinal plate fins: demonstration, modeling and application to thermal storage. Int J Heat Mass Tran 2015;86:465–77.
[19] Yan Z, et al. Performance enhancement of cylindrical latent heat storage units in hot water tanks via wavy design. Renew Energy 2023;218:119282.
[20] Punniakodi BMS, Suyambazhahan S, Senthil R. An experimental study of melting behavior of the phase change material in cylindrical capsules for thermal energy storage. J Energy Storage 2024;81:110492.
[21] Fekadu B, Assaye M. Enhancement of phase change materials melting performance in a rectangular enclosure under different inclination angle of fins. Case Stud Therm Eng 2021;25:100968.
[22] Sharma A, Kothari R, Sahu SK. Effect of fin location on constrained melting heat transfer of phase change material in a spherical capsule: a numerical study. J Energy Storage 2022;52:104922.
[23] Shockner T, Ziskind G. Experimental and numerical evaluation of phase-change material performance in a vertical cylindrical capsule for thermal energy storage. Appl Therm Eng 2023;219:119519.
[24] Safari V, et al. Thermal performance investigation of concentric and eccentric shell and tube heat exchangers with different fin configurations containing phase change material. J Energy Storage 2021;37:102458.
[25] Pahamli Y, et al. Effect of nanoparticle dispersion and inclination angle on melting of PCM in a shell and tube heat exchanger. J Taiwan Inst Chem Eng 2017;81:316–34.
[26] Yang K, et al. Effects of thermophysical properties on optimal selection of phase change material for a triple tube heat exchanger unit at different time scales. J Energy Storage 2023;61.
[27] Wu Y, et al. Numerical investigation of the impact of toothed fins on the heat transfer performance of a shell-and-tube exchanger during phase change material melting process. Int J Heat Mass Tran 2023;217.
[28] Kundu R, et al. A thermal modelling of triple tube heat exchanger using phase change material. Mater Today Proc 2024;102:305–11.
[29] Kumar A, Verma P, Varshney L. An experimental and numerical study on phase change material melting rate enhancement for a horizontal semi-circular shell and tube thermal energy storage system. J Energy Storage 2022;45:103734.
[30] Fadl M, Eames PC. Numerical investigation of the influence of mushy zone parameter Amush on heat transfer characteristics in vertically and horizontally oriented thermal energy storage systems. Appl Therm Eng 2019;151:90–9.
[31] Jones BJ, et al. Experimental and numerical study of melting in a cylinder. Int J Heat Mass Tran 2006;49(15–16):2724–38.
[32] Liu Z, et al. Numerical modeling and parametric study of a vertical earth-to-air heat exchanger system. Energy 2019;172:220–31.
[33] Xiao X, Zhang P. Numerical and experimental study of heat transfer characteristics of a shell-tube latent heat storage system: Part II – discharging process. Energy 2015;80:177–89.
[34] Liu Z, et al. Experimental and numerical study of a vertical earth-to-air heat exchanger system integrated with annular phase change material. Energy Convers Manag 2019;186:433–49.
[35] Memon A, Mishra G, Gupta AK. Buoyancy-driven melting and heat transfer around a horizontal cylinder in square enclosure filled with phase change material. Appl Therm Eng 2020:181.
[36] Spengler FC, Oliveski RDC, Eberhardt GES. Effect of proportions of fins with radial branches on the lauric acid melting process in an annular cavity. Energy 2022;255:124557.
[37] Ezzat Y, Sakr RY, Abdel-Rehim AA. Numerical investigation of the effect of thermal expansion coefficient and mushy zone constant on modelling of the phase change process to provide reliable selection criteria of modelling parameters. J Energy Storage 2023;72:108771.
[38] Hosseinizadeh SF, et al. Unconstrained melting inside a sphere. Int J Therm Sci 2013;63:55–64.
[39] Yan Z, et al. A hybrid method for modeling the unconstrained melting of phase change material in hot water tanks. Energy Build 2022;265:112082.